Polar-Direct-Drive Simulations and Experiments

Introduction

Polar direct drive (PDD)[1] provides a viable path for direct-drive ignition on the National Ignition Facility (NIF).[2] Ideally, direct-drive ignition experiments require a symmetric arrangement[3–5] of high-powered UV laser beams pointed at the target center with focal spots that fill and overlap the spherical target surface. The NIF will be configured initially for x-ray drive, however, with the beams arranged around the polar axes to illuminate the interior of cylindrical hohlraums via entrance holes located at either end of the cylinder.[6] The PDD concept will enable direct-drive ignition experiments on the NIF while it is in the x-ray-drive configuration. Polar direct drive achieves uniform drive by repointing the beams, designing the on-target spot shapes with customized phase plates,[7,8] employing an optional CH ring that surrounds the equatorial region and acts as a plasma lens, refracting laser energy back toward the target (referred to as the Saturn target, see Ref. 9), and taking advantage of the NIF's flexible pulse-shaping capability.

The PDD concept is currently under experimental investigation on the OMEGA Laser System.[8] The goal of the experiments was to provide an understanding (both experimentally and through simulation) of the laser absorption characteristics resulting from repointing the beams and to test the ability to drive PDD implosions that obtain yields close to energy-equivalent symmetric-drive implosions. The common CH targets provide an adequate test bed for this purpose. (Surrogate cryogenic targets that scale to NIF designs are being planned for future experiments.) As shown in Fig. 105.45(a), a 40-beam subset of the 60-beam OMEGA laser has been chosen to emulate the NIF x-ray-drive configuration. Both the standard PDD and Saturn target designs utilize the OMEGA laser in this 40-beam configuration. Figure 105.45(b) illustrates how the beams are repointed for OMEGA PDD experiments. The Saturn target[9] employs an equatorial CH ring to refract laser energy from the obliquely pointed beams toward the target equator. Radiation from the CH ring also plays a role in driving the equator. The initial simulation and evaluation of these experiments was performed using the hydrodynamics code *SAGE*.[10] Present work uses the hydrodynamics code *DRACO*,[11] an arbitrary Lagrangian Eulerian (ALE) code that includes both radiation transport and fusion particle production and transport as well as a full 3-D laser ray-trace deposition package. *DRACO* can also be configured to run in a sliding-grid Eulerian mode (which is necessary to simulate the Saturn targets to support the shock transit in the space between the CH ring and the target).

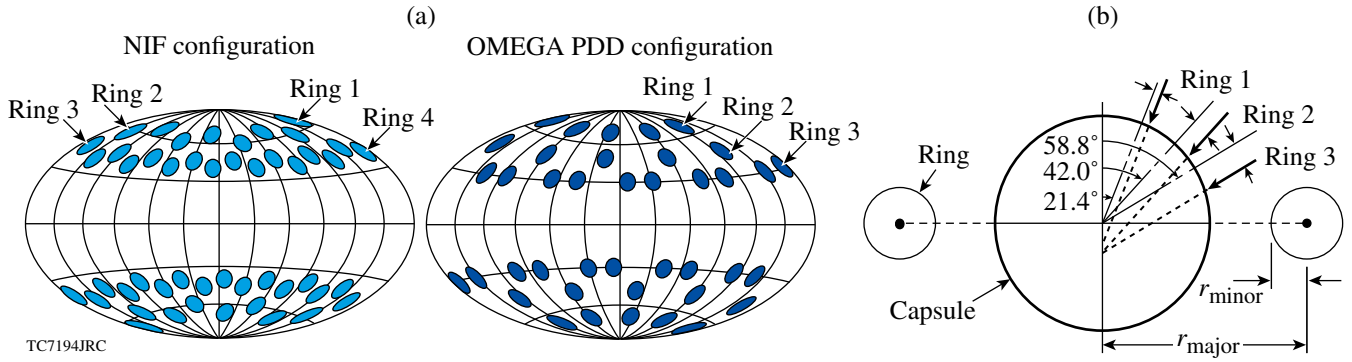

Figure 105.45
(a) Illustration of beam port positions for the NIF and OMEGA indirect-drive configurations. A 40-beam subset of the 60-beam OMEGA Laser System emulates the NIF indirect-drive configuration. (b) The beam pointing schemes described in this paper for the OMEGA PDD program. Rings 1 and 2 (each hemisphere) have five beams each, while Ring 3 (each hemisphere) has ten beams for a total of forty beams. All beams in a ring are offset in the far-field plane perpendicular to the central beam axis (as indicated by the thin arrows) by the amount shown in Table 105.II. The placement of the Saturn ring is also indicated (not to scale).

In **OMEGA Experiments and Simulations** (p. 42), OMEGA PDD experiments and simulations are presented and compared for both types of PDD targets. The *DRACO* simulations of the OMEGA experiments presented here analyze the low-ℓ-mode behavior due to beam overlap and the increased refractive losses due to repointing the beams toward the equator. The angular resolution used in these simulations was 80 zones over a 90° wedge; the low-ℓ-mode structure up to mode $\ell = 22$ is adequately resolved. (Note: there is only significant power in modes up to $\ell = 6$.) The long-wavelength effects of energy balance and beam mispointing as well as the short-wavelength behavior of single-beam nonuniformity are currently under investigation. Good agreement is found by comparing x-ray framing-camera images with *DRACO* simulations. These implosions were all simulated in the sliding-grid Eulerian mode to make a consistent comparison with the Saturn simulations that require Eulerian hydrodynamics.

In **NIF Simulations** (p. 46), substantial gain is predicted with NIF-scale, 2-D *DRACO* implosion simulations. The simulated standard PDD targets consist of cryogenically layered deuterium–tritium (DT) encased with a wetted hydrocarbon (CH) foam[12,13] and a thin CH overcoat layer. The *DRACO* simulations for the NIF also included the effect of the low-ℓ-mode behavior due to beam overlap and repointing and were simulated in the ALE mode. For 1.36 MJ of laser energy, the PDD target gives a gain of 20. In comparison, the gain is 33 if the same target is driven symmetrically with 1.0 MJ of laser energy. The compressed core near stagnation consists of a 40-μm-radius, 10-keV region with a neutron-averaged ρr of 1270 mg/cm^2. The importance of maintaining both shell and shock-front uniformity is stressed.

OMEGA Experiments and Simulations

Experimental confirmation of 2-D *DRACO* hydrodynamic simulations has been obtained by making comparisons with PDD implosions[14] carried out on OMEGA. The implosions were performed with a nominal room-temperature target consisting of 865-μm-diam, 19.7-μm-thick (experimental average) glow-discharge polymer shells filled with D_2 gas at a pressure of 15 atm. This type of target has been used extensively on OMEGA.[10,15–17] All capsules were coated with 500 Å of Al to act as a gas retention barrier and are held in place by 17-μm boron fibers glued to the target surface. (Note that the Al layer and boron fibers were not simulated.) The capsule diameters were measured to an accuracy of 1 μm and the shell thickness to 0.2 μm. The Saturn targets reported here consisted of the same capsule supported by three 10-μm-diam alumina "spokes" (which were not simulated), again glued to the target surface, inside a CH ring of circular cross section with a 1.1-mm major radius and a 150-μm minor radius (shots with a 1.25-mm major radius were also measured but not simulated). The laser drive was a 1-ns flat pulse with ~390 J per beam employing 1-THz, 2-D smoothing by spectral dispersion[18–21] with polarization smoothing.[17] The 40 OMEGA beams were repointed for PDD with a typical accuracy of 15-μm rms using the technique described by Forties and Marshall (Ref. 22). Figure 105.45(b) depicts the beam-pointing scheme used for the experiments and simulations described in this work. Table 105.II details the configurations, giving the lateral offsets from the central beam axis in the far-field plane for three different cases. Figure 105.45(b) also indicates the placement of the Saturn ring.

Table 105.II: PDD offsets, Δr (μm)

	Case	Ring 1	Ring 2	Ring 3
A	Shot 38502 Shot 39281	90	120	120
B	Shot 34669	91	188	196
C	Proposed	74	61	180

As in Refs. 10 and 14, the imploding targets were diagnosed by framed x-ray backlighting. The framing cameras were configured to operate at a magnification of 6 with 10-μm pinholes and an effective resolution of ~11 μm. Each frame's integration time was ~50 ps and the absolute time of a frame was determined by noting the time of backlighter onset (known to be better than 10 ps). Au backlighters were used with a broadband emission ranging from 2.2 to 2.5 keV. Two backlighters were available, one viewing the target from just below the equator ($\theta_{va} = 101°$) and one well above the equator ($\theta_{va} = 63°$). The latter provided a view of the partially imploded plasma even in the presence of a Saturn ring. The delay of the backlighter beams was +0.9 ns relative to the beginning of the laser pulse. All beams used the same 1-ns flattop pulse shape with 100-ps rise and fall times. Peak power occurred from 0.1 ns to 1.0 ns. Backlit radiographs were obtained after the end of the drive pulse (~1.1 ns to 1.7 ns). Stagnation occurs around 1.9 ns.

X-ray radiography was used to measure the magnitude of deviations from spherical symmetry. Early in time, the deviations from sphericity are small and the streaked and framed x-ray imaging shows that the shell trajectory closely matches the predictions of 1-D simulations.[10] Later in time, however, the deviations become larger and increasingly important. The evolution of the shell distortion can be seen in Fig. 105.46(a), where three backlit framed x-ray images taken at times t = 1.23, 1.49, and 1.68 ns are shown for OMEGA shot 38502

(19.6-μm CH shell thickness), as viewed from the angle θ_{va} = 101°. This shot utilized the pointing intended for a Saturn target (case A of Table 105.II) but the target was shot without the external CH ring; therefore, strong distortions were expected around the equatorial plane where the target was underdriven. The *DRACO* simulation of this experimental shot was post-processed with the code SPECT3D (Ref. 23) to simulate an x-ray backlighter at the same viewing angle. The *DRACO*/SPECT3D-simulated x-ray radiograph results of shot 38502 are shown in Fig. 105.46(b) at times corresponding to the experimental images. Both the size and shape of the simulated radiographs are close to those observed.

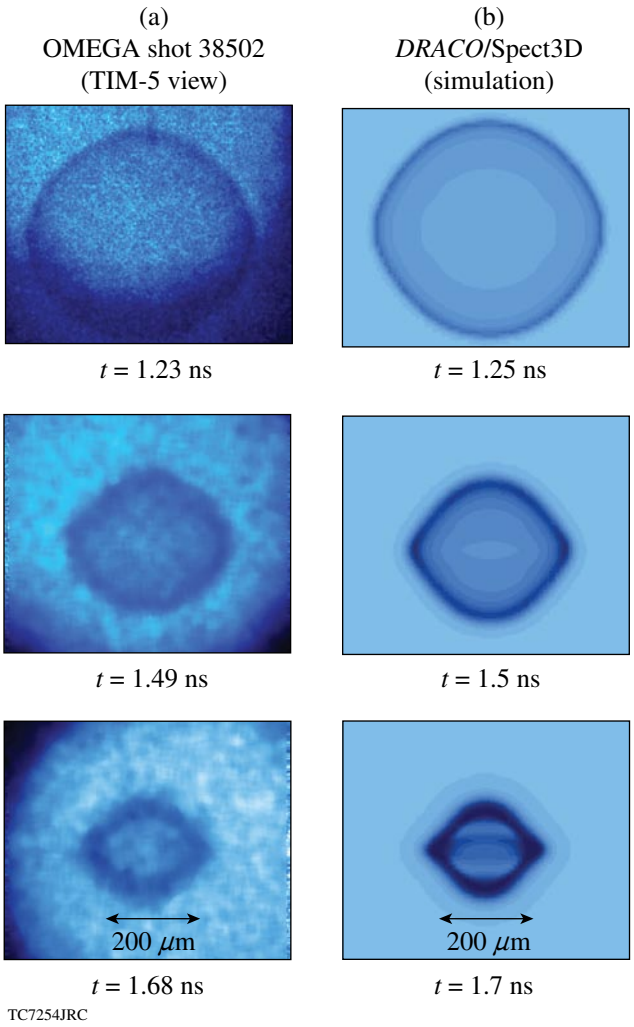

Figure 105.46
(a) Experimental x-ray framing-camera images. The dark rings (minimum x-ray transmission) indicate the evolution of the shell distortion. The times t = 1.2, 1.5, and 1.7 ns are shown for a standard PDD target on OMEGA for shot 38502. (b) Simulated x-ray radiographs at corresponding times produced from *DRACO* simulations that have been post-processed by SPECT3D. Note that the pointing used for this shot is intended for a Saturn target. The radiographs are imaged from TIM-5 at θ_{va} = 101°.

To provide a quantitative comparison between simulations and experiments, the locations of the x-ray radiograph minima of an OMEGA experiment and the simulated x-ray radiograph from a *DRACO*/SPECT3D simulation can be plotted [as a function of angle (θ') from the vertical image axis]. The x-ray radiograph minima of OMEGA shot 38502 at the viewing angle θ_{va} = 63° as a function of angle (θ') are shown in Fig. 105.47(a) (circles) taken at 1.68 ns, which was extracted from the x-ray radiograph shown in Fig. 105.47(b). The typical error in determining the position of the minimum is ±2 μm, as indicated by the example error bar in Fig. 105.47(a).

The data points extracted from a simulated radiograph are sufficiently smooth that they are well represented by a Legendre polynomial fit. These data are also extracted with

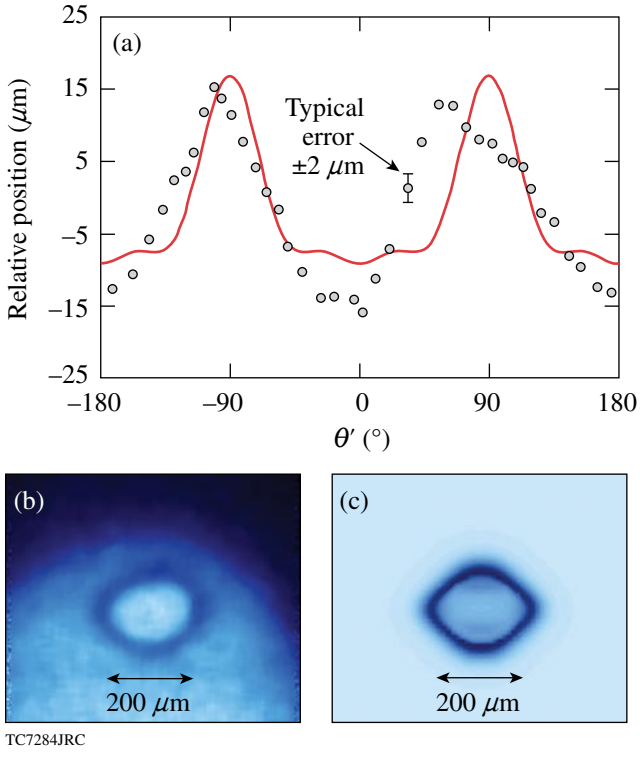

Figure 105.47
(a) The radii of the x-ray transmission minimum as a function of image polar angle (θ') are shown for OMEGA standard-PDD shot 38502 as circles at 1.68 ns relative to a radius of 93.1 μm. A Legendre polynomial fit to the simulated radiograph data is displayed as the black line at 1.7 ns relative to a radius of 94.3 μm. The peak-to-peak deviations are 15 μm for the experimental data and 13 μm for the *DRACO*/SPECT3D simulation. (b) The experimental and (c) simulated radiographs. The radiographs are imaged at θ_{va} = 63°.

an error of ±2 μm. Since the imploding shells are observed at an angle to the symmetry axis, it is necessary to transform the image's polar angle into the natural coordinates of the Legendre modes, viz.

$$\cos(\theta) = \cos(\theta')\sin(\theta_{va}), \tag{1}$$

where θ is the polar angle of the spherical coordinate system aligned with the target pole and θ_{va} is the viewing angle used in the experiment. The Legendre decomposition over the first six modes is given by

$$R_{\exp}(\theta') = \sum_{l-1}^{6} A_l \cdot P_l[\cos(\theta)], \tag{2}$$

where P_l is the Legendre polynomial of order l. This fit approximates the shape of the radiograph to that of a cut through an idealized thin shell. No significant modes above $\ell = 6$ were found, so only the fits up to 6 were included. A Legendre polynomial fit to the transmission minima from the *DRACO*/SPECT3D-simulated x-ray radiograph [Fig. 105.47(c)] is found and plotted in Fig. 105.47(a) (thick line) for the simulation time of 1.7 ns. The peak-to-peak deviations are 15 μm for the experimental data and 13 μm for the *DRACO* simulation.

The framed x-ray radiographs for a Saturn target taken at times t = 1.21, 1.46, and 1.65 ns for OMEGA shot 39281 (19.7-μm shell thickness) are shown in Fig. 105.48(a) with the same beam pointings (case A of Table 105.II). *DRACO*/SPECT3D-simulated x-ray radiographs are shown in Fig. 105.48(b) at similar times. Lineouts as a function of θ', similar to those of Fig. 105.47(a), are shown at ~1.65 ns in Fig. 105.49 with the experimental data as circles and the *DRACO*/SPECT3D data as a solid line. The peak-to-peak deviations are 10 μm for the raw data and 9 μm for the *DRACO* simulation. The effect of the external CH ring is readily observed by noting that the equatorial bulge around the equator has been decreased [compare Figs. 105.46 and 105.48 and Figs. 105.47(a) and 105.49] because of increased laser-energy deposition and radiation from the CH ring, which together increase the drive in the equatorial region.[10]

Saturn targets have obtained the best experimental yields to date relative to energy-equivalent, 60-beam symmetrically driven targets. The measured DD neutron yields for both types of PDD targets (standard and Saturn) and, for comparison, the yields obtained from symmetrically irradiated targets (60 beams with an equivalent on-target energy of 15.3 kJ) are

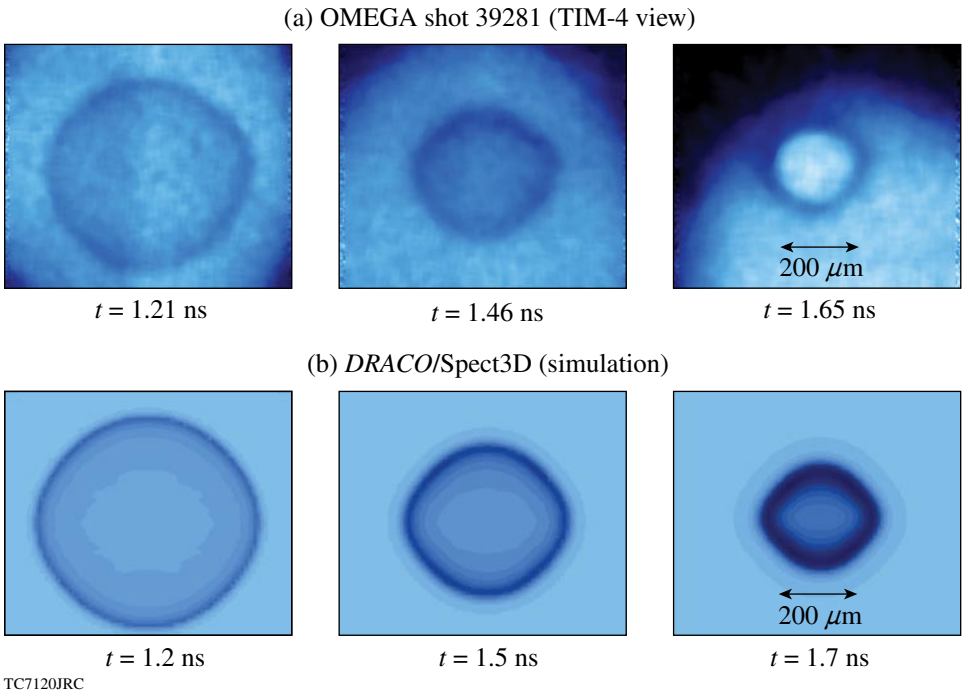

Figure 105.48
(a) Experimental x-ray framing-camera images indicating the evolution of the shell for a Saturn target on OMEGA shot 39281 at times t = 1.2, 1.5, and 1.7 ns. (b) Simulated x-ray radiographs using *DRACO* and SPECT3D. The radiographs are imaged at θ_{va} = 63°.

shown in Fig. 105.50. The standard targets obtained ~35% of the symmetric target yields. The spoke-mounted Saturn targets obtained about 75% of the symmetric target yields. The *DRACO*-simulated yield for the energy-equivalent symmetric-drive shot 34644 (19.6-μm shell thickness) was 2.91×10^{11} DD neutrons. This compares to the simulated yields for the standard PDD shot 34669 (19.3-μm shell thickness) and the Saturn shot 38291, 1.28×10^{11} and 1.73×10^{11} DD neutrons, respectively. The normalized yield results for two shots are summarized in Table 105.III. The Saturn target simulation yield increased relative to the standard PDD target but only by 34%, from 44% to 59%, whereas the experimental yield doubled (when comparing the standard PDD to the Saturn target).

Standard PDD targets can benefit from further optimization of pointing, spot shapes, and ring energy balance to produce results comparable to the current Saturn target designs. The benefit of finding an optimized standard-PDD design is the ability to fabricate and shoot a cryogenic PDD target. The Saturn design is not practical for cryogenic targets. For the sake of comparison, a warm CH target is used here since current experimental and simulated results exist. The current pointings used for standard PDD (case B in Table 105.II) were chosen on the basis of the existing phase plates on OMEGA (super-Gaussian of order 3.7). An optimization algorithm (separate from *DRACO*) was run that automatically tunes the beam pointing and spot shapes for equal energy beams, given an absorption angular spectrum extracted from a *DRACO* simulation under similar conditions. Different results will be

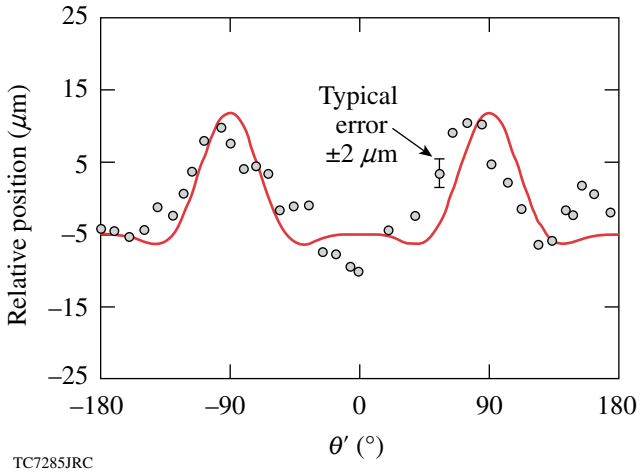

Figure 105.49
The radius of the x-ray transmission minimum as a function of image polar angle (θ') extracted from the 1.65-ns (right-hand) image of Fig. 105.48(a), shown as circles, relative to a radius of 101.7 μm. A Legendre polynomial fit to the simulated radiograph data extracted from the 1.7-ns (right-hand) image of Fig. 105.48(b) is displayed as the solid line relative to a radius of 106.6 μm. The peak-to-peak deviations are 10 μm for the experimental data and 9 μm for the *DRACO* simulation.

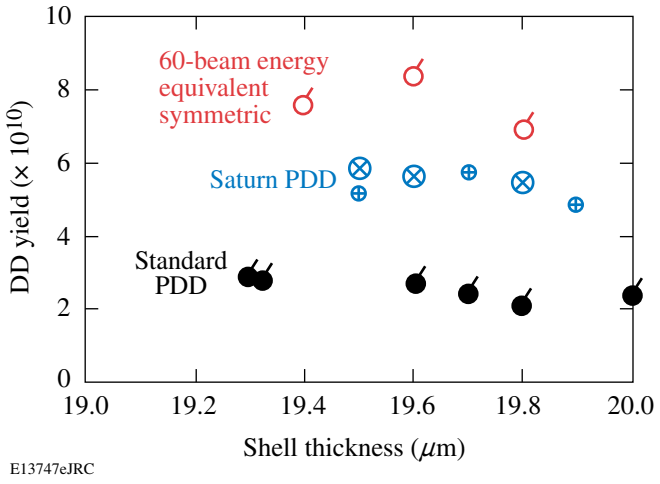

Figure 105.50
The measured DD neutron yields for both types of PDD targets (standard and Saturn) and, for comparison, the yields obtained from symmetrically irradiated targets (60 beams with the same on-target energy of 15.3 kJ). The standard-PDD targets obtained ~35% of the symmetric target yields. The Saturn targets obtained about 75% of the symmetric target yields. All shots employed a 1-ns flattop pulse with 100-ps rise and fall times. All PDD targets used optimal beam pointing ("A" of Table 105.II for Saturn, "B" for standard PDD). The Saturn shots with different major diameters are as indicated on the plot; the small symbols correspond to $r_{major} = 1100$ μm and the large symbols correspond to $r_{major} = 1250$ μm.

Table 105.III: Normalized experimental and simulation yields. The experimental yields are normalized to the energy-equivalent symmetric-drive experiment for shot 34644. The simulation yields are normalized to the simulation of the energy-equivalent symmetric-drive simulation.

	Standard PDD shot 34669	Saturn shot 39281 spoke mount
Experimental yield normalized to symmetric shot 34644	0.35	0.69
Simulation yield normalized to simulation of symmetric shot 34644	0.44	0.59

obtained by making alternate choices of sampled absorption spectra. The nonuniformity during the acceleration phase plays an important role for the long-wavelength distortions characteristic of PDD, especially when the laser energy is absorbed farther away from the critical surface around the equator. For this reason, the angular dependent absorption is taken during the acceleration phase at ~700 ps with the assumption that it is representative of the most influential period. The optimization process first overlaps the beams onto a hard sphere while accounting for the angular dependence of absorption. The spot shapes are changed and also repointed to minimize the nonuniformity of the absorbed energy profile on the surrogate target sphere. The resultant pointing for the different beam rings is 74, 61, and 180 μm. The resulting spot shapes are super-Gaussians of orders 2.58, 2.11, and 2.42, respectively, with 5% intensity contours located at 1.05× the target radius. Optimal PDD designs tend toward lower super-Gaussian orders because the narrower intensity peaks give the rings more independent control, particularly in the troublesome equatorial region; e.g., more energy can be delivered to the equator with minimal influence on the rest of the target. Additionally, the spot shapes are modulated by an order-10 super-Gaussian envelope with a 5% intensity contour at the target radius to maximize the energy delivered to the target (especially by minimizing the over-the-horizon energy near the equator). The energy of the first ring was derated by 15% to prevent overdrive in the polar region; as a consequence, the incident laser energy is only 14.8 kJ. The simulated absolute yield for this proposed configuration is comparable to that of the Saturn design (using 15.6 kJ of laser energy), and the symmetry of the shell is very similar, as shown in Figs. 105.51(a) and 105.51(b). It is expected that the shell symmetry can be improved by further tuning the beam repointing and spot shapes. The yields relative to the simulation of the energy-equivalent symmetric-drive target are 59% and 58%, respectively.

NIF Simulations

Cryogenic, DT-filled, wetted CH-foam targets show great promise for high PDD gains on the NIF.[24] The four rings of beams in the NIF indirect-drive configuration shown in Fig. 105.45(a) are repointed into three rings which are logically grouped by the angle in which the beam centers intersect the initial target radius; they are designated as polar, midlatitude, and equatorial rings. The polar and midlatitude rings are typically not repointed by a significant amount, whereas the equatorial ring is repointed the most, amounting to a transverse shift in the far-field plane of ~850 μm.

A successfully igniting PDD target requires that both shell and shock-front uniformity be maintained at a high level throughout the drive pulse. The equator experiences the highest incident angles, which lead to higher refractive losses and lower hydrodynamic efficiency, 2-D effects such as lateral mass and heat flow become important, and the relative pointing changes as the critical surface moves inward. The shell uniformity can be compromised because of the dynamic nature of the low-ℓ-

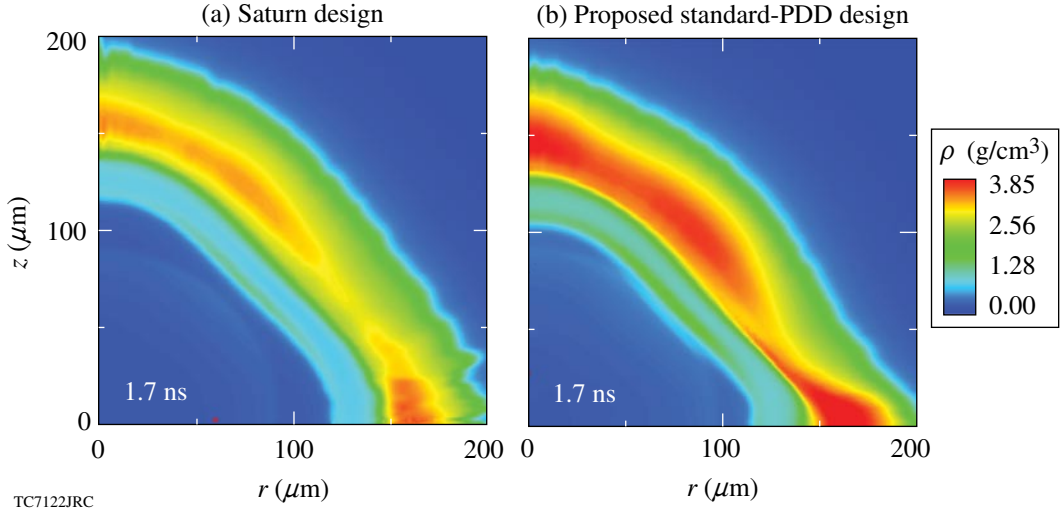

Figure 105.51
(a) The mass density for the OMEGA Saturn configuration near stagnation at 1.7 ns. (b) The mass density for the proposed OMEGA standard PDD configuration at 1.7 ns and the same distance traveled. The yields relative to the simulation of the energy-equivalent symmetric target are 59% and 58%, respectively. The axis of symmetry is along the vertical axis; i.e., the pole is pointing upward.

mode distortions inherent in the PDD setup. Their effect can be controlled, however, through sufficient overall drive uniformity. The uniformity can be optimized through beam pointing, spot shape designs, and time-dependent pulse shaping. The energy deposited near the equator must be increased to compensate for the higher refractive losses (lower energy absorption) and lower hydrodynamic efficiency (due to the laser energy being deposited farther out in the corona). This can be accomplished by using elliptical spot shapes and/or higher power in the equatorial rings.[25] The level of shock-front uniformity determines the symmetry of the shock-heated core and cannot be ignored. An improperly timed shock front can cause a design to fail because of a small and distorted shock-heated hot spot, whereas small adjustments during the foot pulse can make the same target ignite by developing a large and minimally distorted hot spot.

The NIF PDD target presented here is based on a 1.0-MJ, symmetric-drive, cryogenic, DT-filled, wetted CH-foam target with a thin CH overcoat that obtains a gain of 33. The interior DT vapor layer is 1380 μm in radius. The cryogenic DT ice layer is 180 μm thick. The wetted CH-foam layer is 70 μm thick and is modeled by a uniform mass density of 0.392 g/cm^3. A thin CH layer overcoats the target and is 1.2 μm thick. The 1.0-MJ pulse shape used for this target is plotted in Fig. 105.52(a).

For the *DRACO* simulation of the cryogenic, DT-filled, wetted CH-foam target reported here, all the rings have the same primary spot shape: a low super-Gaussian order of 2.2. A secondary elliptical super-Gaussian of the same order is superimposed on the equatorial beams. It has an ellipticity of 5, a relative strength (compared with the primary spot shape) of around 0.45, and a relative shift of 0.15 times the initial target radius. An equation for the composite equatorial spot can be written as

$$I_{\text{eq}} = e^{\alpha\left(x^2+y^2\right)^{\text{sg}/2}} + 0.45e^{\alpha\left\{\left[5\left(x-0.15\,r_t\right)\right]^2+y^2\right\}^{\text{sg}/2}}, \tag{3}$$

where $\alpha \equiv \ln(0.05)/r_t^{sg}$, sg $\equiv 2.2$, and r_t is the initial target radius. The secondary ellipse increases the energy deposition near the equator.

Beam repointing, spot shapes, and the relative pulse strengths of the different beams determine the in-flight shell uniformity. Initial guesses of the spot positions and the spot shapes are found off-line from *DRACO* using the same optimization technique mentioned in the previous section. Fine-tuning of the beam pointing takes place by running further *DRACO* simulations. The repointings used for the simulations presented here are 23.5°, 44.5°, and 80° for the polar, midlatitude, and equatorial rings, respectively.

An active pulse-shape optimization process internal to *DRACO* is then invoked to determine the relative pulse strengths at each ring by minimizing shell nonuniformity throughout the simulations. The optimized pulse shapes divide roughly into two separate temporal regions: the foot and the main drive. During the foot, the conduction zone is relatively uniform and does not require a large amount of compensation near the equator for a drive similar to the pole. Thus, the relative strengths between the ring pulse shapes are not very dif-

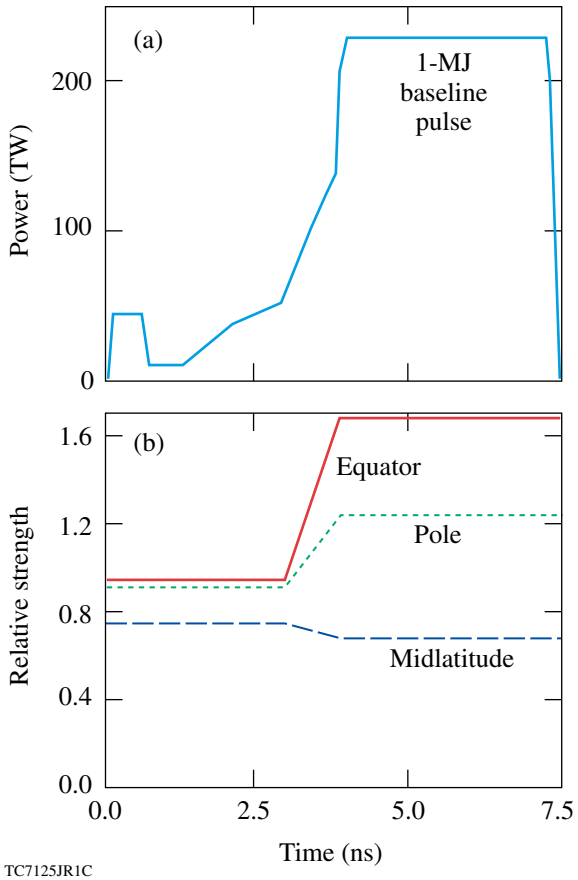

Figure 105.52
(a) Baseline 1.0-MJ pulse designed for a symmetrically driven NIF target. (b) Time-dependent multipliers giving the relative strengths of the three rings of beams (pole, midlatitude, and equator) in a standard PDD configuration. The three PDD pulses (baseline pulse multiplied by the relative strengths) represent 1.36 MJ overall.

ferent. (Fine-tuning for the shock front will still be required.) As the main pulse ablates the shell at a higher rate, however, the conduction zone becomes progressively nonuniform with the greatest standoff distance (separation distance between the energy deposition region and the ablation surface) occurring near the equator, and, consequently, the relative strengths between the ring pulse shapes are different with the most power given to the equatorial ring. The pulse shapes are then smoothed and fine-tuning takes place by adjusting the relative strengths after observing the shell and shock-front distortions during *DRACO* simulations. The main trend of the optimized pulse shapes increases the power in the equatorial beams relative to the other beams during the main drive. The smoothed pulse shapes vary continuously, which makes it difficult to adjust the relative factors between the different pulse shapes for each ring. It is found that using constant relative strengths in the foot that change to new constant factors during the main drive is adequate to tune the pulse shapes. The constant relative strengths in the foot and main drive sections of the pulse are initially chosen as the average value of the optimized pulses in each separate period. The constant relative strengths in the two sections of the pulse are independently adjusted to fine-tune the shell and shock-front uniformity.

Maintaining both the shell and shock-front uniformity is critical to obtaining substantial gains. Correcting only for the shell distortions can have a detrimental side effect of distorting the shock front. If the shock front is distorted, nonuniform shock heating produces a misshaped and small hot spot (defined here as the 10-keV temperature contour, which does not necessarily reflect the uniformity of the shell), leading to a failed target. The shell can have adequate uniformity at stagnation but with a severely distorted and small hot spot. When compared to a simulation that ignites, the 10-keV hot spot is large and conformal to the shell.

The application of this design process is given here for an igniting NIF PDD target with the parameters given in the beginning of this section. The symmetric-drive target and 1.0-MJ baseline pulse in Fig. 105.52(a) are used as a guide for tuning the ring pulse shapes by requiring that the shell trajectory matches that of the symmetric case as close as possible. In addition, the shock-front uniformity must be high enough to produce a large hot spot. The constant multiplication factors of each of the three rings resulting from the optimization algorithm described above are calculated first based on the optimized spot shapes and ring repointings found outside of *DRACO*. Then the constant factors in the main pulse are adjusted to closely match the trajectory of the symmetric-drive case while also obtaining the best overall low-ℓ-mode shell uniformity. Since only the pulse strengths of the three rings can be adjusted, a limited range of ℓ modes can be controlled (typically $\ell \leq 8$). Once the shell uniformity is tuned, the relative shock strengths are tuned using the foot portion to improve the shock-front uniformity. The shell uniformity is not greatly affected by the typical adjustments needed during the foot to compensate for shock-front distortions. By this point the shock front has roughly the same symmetry as the shell but still needs improvement. It is adequate to compare the shock positions of the pole relative to the equator. The relative shock positions as a function of time with and without shock-front adjustments are plotted in Fig. 105.53. The fine-tuning of the shock-front uniformity aligns the shock front prior to ignition. Without the fine tuning, the misalignment is about 20 μm at 8.0 ns, whereas the tuned shock front achieves almost perfect alignment. The multiplication factors found after the complete tuning process are plotted in Fig. 105.52(b).

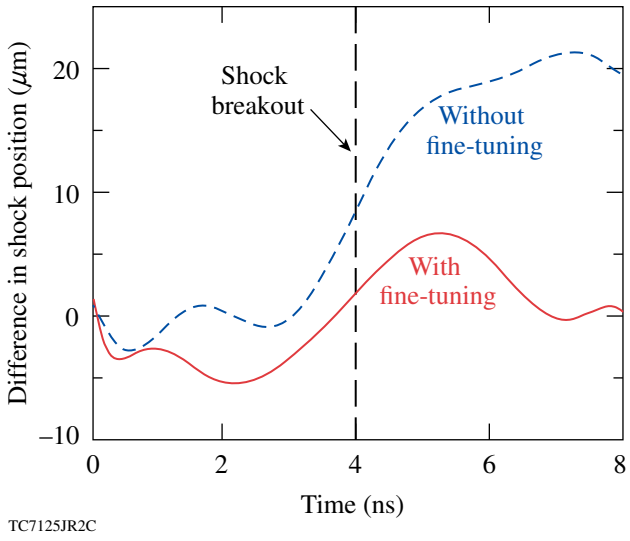

Figure 105.53
Relative shock positions (shock position along the pole minus shock position along the equator) as a function of time with and without fine-tuning of the shock front for the NIF simulations. The dashed line is without fine-tuning. The solid line is after fine-tuning the shock front. The case with fine-tuning ignites.

A *DRACO* simulation in ALE mode was run for the PDD cryogenic, DT-filled, wetted CH-foam target on a 90° wedge. The angular resolution used in the simulations was 60 zones over a 90° wedge; the low-ℓ-mode structure up to mode ℓ = 16 is adequately resolved. The simulation used the 23.5°, 50°, and 80° pointings for the polar, midlatitude, and equatorial rings. The optimal pulse shapes for the three rings are plotted in Fig. 105.52. Simulated mass density and ion-temperature

profiles near the stagnation of this tuned design, at 8.12 ns, are shown in Fig. 105.54. The 10-keV hot-spot radius is about 40 μm. This simulation produced a gain of 20 using a flux limiter of 0.06 and required 1.36 MJ of laser energy for the PDD configuration compared with the 1.0 MJ required for symmetric drive with a gain of 33. The laser energy is higher because of the required compensation for losses at the equator.

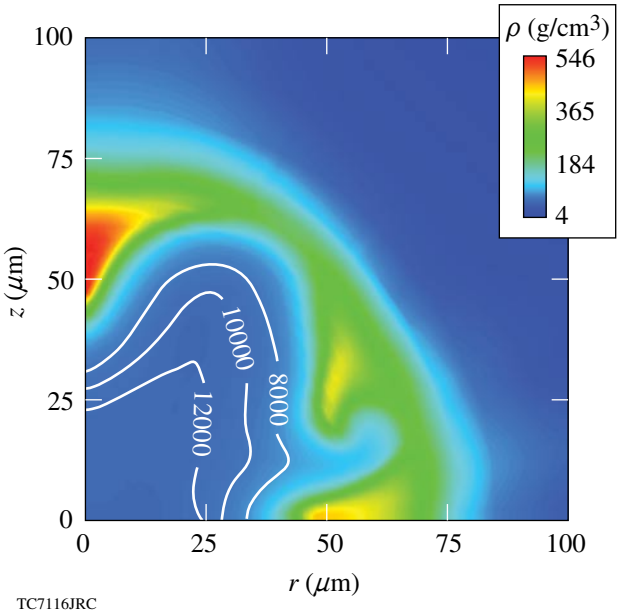

Figure 105.54
Mass density ρ and ion temperature contours in electron volts calculated by *DRACO* for a cryogenic, DT-filled, wetted CH-foam PDD target irradiated with 1.36 MJ of laser energy. The temperature contours show the formation of a ~40-μm-radius hot spot. This simulation predicts a gain of 20. The axis of symmetry is along the vertical axis; i.e., the pole is pointing upward.

Conclusions

The *DRACO* simulations of both standard-PDD and Saturn targets agreed well with the experiments during the acceleration phase by observing the characteristics of the shell evolution in the experimental and simulated x-ray radiographs. The simulations also showed the same trend as the experiments in that the Saturn targets produced higher yields than the standard-PDD targets using the existing phase plates on OMEGA (super-Gaussian of the order of 3.7). An optimized standard-PDD design was proposed that used customized phase plates, different pointings and power balance, and was able to produce a yield on par with the current Saturn design but with 5% less incident energy. Further optimization of OMEGA standard-PDD designs is expected and is currently under investigation using the techniques described here and also by employing a shimmed CH ablator on the target.

A 1.36-MJ, cryogenic DT, standard-PDD design for the NIF using the same targets as the 1.0-MJ symmetric-drive design ignited and produced a gain of 20 in a *DRACO* simulation. The PDD design employed customized phase plates, optimized beam repointings, and tuned pulse shapes for the polar, midlatitude, and equatorial rings. Maintaining a high level of shell and shock-front uniformity is found to be critical to obtaining substantial gains. Further simulations are under investigation to test the robustness of this design by including the effects of mispointing, power imbalance, and short-wavelength perturbations.

ACKNOWLEDGMENTS

This work was supported by the U.S. Department of Energy Office of Inertial Confinement Fusion under Cooperative Agreement No. DE-FC52-92SF19460, the University of Rochester, and the New York State Energy Research and Development Authority. The support of DOE does not constitute an endorsement by DOE of the views expressed in this article.

REFERENCES

1. S. Skupsky, J. A. Marozas, R. S. Craxton, R. Betti, T. J. B. Collins, J. A. Delettrez, V. N. Goncharov, P. W. McKenty, P. B. Radha, T. R. Boehly, J. P. Knauer, F. J. Marshall, D. R. Harding, J. D. Kilkenny, D. D. Meyerhofer, T. C. Sangster, and R. L. McCrory, Phys. Plasmas **11**, 2763 (2004).
2. J. Paisner *et al*., Laser Focus World **30**, 75 (1994).
3. P. W. McKenty, V. N. Goncharov, R. P. J. Town, S. Skupsky, R. Betti, and R. L. McCrory, Phys. Plasmas **8**, 2315 (2001).
4. E. M. Campbell and W. J. Hogan, Plasma Phys. Control. Fusion **41**, B39 (1999).
5. J. D. Lindl, *Inertial Confinement Fusion: The Quest for Ignition and Energy Gain Using Indirect Drive* (Springer-Verlag, New York, 1998), Chap. 6, pp. 61–82.
6. J. D. Lindl *et al*., Phys. Plasmas **11**, 339 (2004).
7. T. R. Boehly, R. S. Craxton, T. H. Hinterman, J. H. Kelly, T. J. Kessler, S. A. Kumpan, S. A. Letzring, R. L. McCrory, S. F. B. Morse, W. Seka, S. Skupsky, J. M. Soures, and C. P. Verdon, Rev. Sci. Instrum. **66**, 508 (1995).
8. J. A. Marozas, "Fourier-Transform-Based, Phase-Plate Design Technique: A High-Pass Phase-Plate Design as an Application for OMEGA and the NIF," submitted to the Journal of the Optical Society of America A.
9. R. S. Craxton and D. W. Jacobs-Perkins, Phys. Rev. Lett. **94**, 095002 (2005).
10. R. S. Craxton, F. J. Marshall, M. J. Bonino, R. Epstein, P. W. McKenty, S. Skupsky, J. A. Delettrez, I. V. Igumenshchev, D. W. Jacobs-Perkins, J. P. Knauer, J. A. Marozas, P. B. Radha, and W. Seka, Phys. Plasmas **12**, 056304 (2005).

11. P. B. Radha, V. N. Goncharov, T. J. B. Collins, J. A. Delettrez, Y. Elbaz, V. Yu. Glebov, R. L. Keck, D. E. Keller, J. P. Knauer, J. A. Marozas, F. J. Marshall, P. W. McKenty, D. D. Meyerhofer, S. P. Regan, T. C. Sangster, D. Shvarts, S. Skupsky, Y. Srebro, R. P. J. Town, and C. Stoeckl, Phys. Plasmas **12**, 032702 (2005).

12. R. A. Sacks and D. H. Darling, Nucl. Fusion **27**, 447 (1987).

13. S. Skupsky, R. Betti, T. J. B. Collins, V. N. Goncharov, D. R. Harding, R. L. McCrory, P. W. McKenty, D. D. Meyerhofer, and R. P. J. Town, in *Inertial Fusion Sciences and Applications 2001*, edited by K. Tanaka, D. D. Meyerhofer, and J. Meyer-ter-Vehn (Elsevier, Paris, 2002), pp. 240–245.

14. F. J. Marshall, R. S. Craxton, M. J. Bonino, R. Epstein, V. Yu. Glebov, D. Jacobs-Perkins, J. P. Knauer, J. A. Marozas, P. W. McKenty, S. G. Noyes, P. B. Radha, W. Seka, S. Skupsky, V. A. Smalyuk, J. A. Frenje, C. K. Li, R. D. Petrasso, and F. H. Séguin, "Polar-Direct-Drive Experiments on OMEGA," submitted to Inertial Fusion Science and Applications 2005.

15. F. J. Marshall, J. A. Delettrez, R. Epstein, V. Yu. Glebov, D. R. Harding, P. W. McKenty, D. D. Meyerhofer, P. B. Radha, W. Seka, S. Skupsky, V. A. Smalyuk, J. M. Soures, C. Stoeckl, R. P. Town, B. Yaakobi, C. K. Li, F. H. Séguin, D. G. Hicks, and R. D. Petrasso, Phys. Plasmas **7**, 2108 (2000).

16. F. J. Marshall, J. A. Delettrez, R. Epstein, R. Forties, R. L. Keck, J. H. Kelly, P. W. McKenty, S. P. Regan, and L. J. Waxer, Phys. Plasmas **11**, 251 (2004).

17. T. R. Boehly, V. A. Smalyuk, D. D. Meyerhofer, J. P. Knauer, D. K. Bradley, R. S. Craxton, M. J. Guardalben, S. Skupsky, and T. J. Kessler, J. Appl. Phys. **85**, 3444 (1999).

18. S. Skupsky, R. W. Short, T. Kessler, R. S. Craxton, S. Letzring, and J. M. Soures, J. Appl. Phys. **66**, 3456 (1989).

19. *LLE Review Quarterly Report* **78**, 62, Laboratory for Laser Energetics, University of Rochester, Rochester, NY, LLE Document No. DOE/SF/19460-295 (1999).

20. S. P. Regan, J. A. Marozas, R. S. Craxton, J. H. Kelly, W. R. Donaldson, P. A. Jaanimagi, D. Jacobs-Perkins, R. L. Keck, T. J. Kessler, D. D. Meyerhofer, T. C. Sangster, W. Seka, V. A. Smalyuk, S. Skupsky, and J. D. Zuegel, J. Opt. Soc. Am. B **22**, 998 (2005); S. P. Regan, J. A. Marozas, J. H. Kelly, T. R. Boehly, W. R. Donaldson, P. A. Jaanimagi, R. L. Keck, T. J. Kessler, D. D. Meyerhofer, W. Seka, S. Skupsky, and V. A. Smalyuk, J. Opt. Soc. Am. B **17**, 1483 (2000).

21. J. A. Marozas, J. Opt. Soc. Am. B **19**, 75 (2002).

22. R. A. Forties and F. J. Marshall, Rev. Sci. Instrum. **76**, 073505 (2005).

23. J. J. MacFarlane *et al*., in *Inertial Fusion Sciences and Applications 2003*, edited by B. A. Hammel, D. D. Meyerhofer, J. Meyer-ter-Vehn, and H. Azechi (American Nuclear Society, La Grange Park, IL, 2004), pp. 457–460; Prism Computational Sciences, Inc., Madison, WI, 53711.

24. S. Skupsky, R. S. Craxton, F. J. Marshall, R. Betti, T. J. B. Collins, R. Epstein, V. N. Goncharov, I. V. Igumenshchev, J. A. Marozas, P. W. McKenty, P. B. Radha, J. D. Kilkenny, D. D. Meyerhofer, T. C. Sangster, and R. L. McCrory, "Polar Direct Drive—Ignition at 1-MJ," submitted to Inertial Fusion Sciences and Applications 2005.

25. S. Skupsky, R. S. Craxton, F. J. Marshall, R. Betti, T. J. B. Collins, R. Epstein, V. N. Goncharov, I. V. Igumenshchev, J. A. Marozas, P. W. McKenty, P. B. Radha, J. D. Kilkenny, D. D. Meyerhofer, T. C. Sangster, and R. L. McCrory, Phys. Plasmas **11**, 276 (2004).